Title: Triple oxygen and clumped isotopes in modern soil carbonate along an aridity gradient in the Serengeti, Tanzania

Authors: Emily J. Beverly[1,2], Naomi E. Levin[2], Benjamin H. Passey[2], Phoebe G. Aron[2], Drake A. Yarian[2], Mara Page[2], and Elise M. Pelletier[2]

[1]University of Houston
Earth and Atmospheric Sciences
3507 Cullen Blvd, Room 214
Houston, TX 77204 USA

[2]University of Michigan
Department of Earth & Environmental Sciences
1100 North University Ave
Ann Arbor, MI 48109 USA

Abstract

The isotopic composition of paleosol carbonates are used extensively to reconstruct past vegetation, climate, and altimetry, but poor constraints on soil evaporation and temperature have limited the utility of oxygen isotopes in the studies. Recent advances in carbonate clumped isotope thermometry ($T_{\Delta47}$) allow for independent controls on temperature, but the influence of evaporation remains unresolved. However, the sensitivity of ^{18}O-^{17}O-^{16}O distributions to kinetic fractionation makes it possible to use triple oxygen isotopes ($\Delta'^{17}O$) to track evaporation in water. Recent work shows the sensitivity of $\Delta'^{17}O$ to evaporation in lakes and lacustrine carbonates, but little is known about variation of $\Delta'^{17}O$ in soil carbonates and their potential to track evaporation. For this study, we sampled soils across an aridity gradient in the Serengeti, Tanzania to evaluate how soil carbonate $\Delta'^{17}O$ tracks soil water evaporation. Modern soil carbonates were collected from 11 sites across a transect of the Serengeti Ecosystem where mean annual precipitation and aridity index range from 499 to 846 mm yr^{-1} and 0.33 to 0.55, respectively. $\delta^{13}C$ values range from -2.7 to 1.8‰ and reflect C_4 dominated grasslands, whereas $\delta^{18}O$ values of soil carbonates vary by ~8‰ along a gradient in aridity. $T_{\Delta47}$ from these soil

carbonates average 23°C (1σ ±4°C), which does not vary significantly across sites or with depth, likely due to minimal annual variation in temperature at the equator. Using these temperatures for each carbonate, reconstructed $\delta^{18}O$ values of soil water are up to 6‰ higher than $\delta^{18}O$ values of local precipitation and springs, indicating considerable soil water evaporation. The $\Delta'^{17}O$ values of these soil carbonates range from -162 to -106 per meg and decrease as both aridity and $\delta^{18}O$ values increase. Our results support the hypothesis that soil water evaporation drives the variance in $\delta^{18}O$ and $\Delta'^{17}O$ of soil carbonate in arid climates, demonstrating the potential for soil carbonate $\Delta'^{17}O$ to track paleoaridity and constrain interpretations of paleosol carbonate $\delta^{18}O$ records.

Keywords
pedogenic carbonate, clumped isotopes, triple oxygen isotopes, evaporation, soil temperature, Africa

Text

1. Introduction

Oxygen and carbon isotopes in pedogenic carbonates are used extensively for reconstructions of past climates, environments, and elevations (e.g., Cerling et al., 2011; Garzione et al., 2008; Levin et al., 2011; Lüdecke et al., 2018; Rech et al., 2019). The carbon isotope composition of soil carbonates ($\delta^{13}C_{sc}$) reflects the proportion of C_3 vs. C_4 plants growing in the soil (Cerling et al., 2011). Interpretations of oxygen isotopes in soil carbonates are less straightforward because $\delta^{18}O$ values of soil carbonate ($\delta^{18}O_{sc}$) depend on both soil temperature and isotopic composition of water associated with carbonate formation, which can vary with the seasonality of soil carbonate formation, ambient temperatures, vegetation cover, $\delta^{18}O$ values of precipitation, and the degree of soil water evaporation (Breecker et al., 2009;

Kelson et al., 2020). Carbonate clumped isotope thermometry (Δ_{47}) has greatly advanced the understanding of how soil temperature and the seasonality of carbonate formation influence $\delta^{18}O_{sc}$ values (Passey et al., 2010; Quade et al., 2013), but many paleoclimate and paleoaltimetry studies are still hampered by the inability to control for the effects of evaporation on $\delta^{18}O_{sc}$ values (e.g., Garzione et al., 2008; Rech et al., 2019).

Recent work shows that triple oxygen isotope (^{16}O, ^{17}O, and ^{18}O) distributions in waters (leaves, lakes, and ponds) and the rock record (carbonates, sulfates, silicates, oxides) are sensitive to evaporation (Bao et al., 2016; Gázquez et al., 2018; Li et al., 2017; Passey et al., 2014; Passey and Ji, 2019; Surma et al., 2018). Although we know that evaporation plays a strong role in soil carbonates, especially in hyper-arid environments where $\delta^{18}O_{sc}$ values are often much greater than predicted using local temperatures and $\delta^{18}O$ of meteoric water ($\delta^{18}O_{mw}$) (e.g., Quade et al., 2007), we currently do not have an independent way to gage soil water evaporation in the rock record. There is tremendous potential to use $\Delta'^{17}O$ in soils to evaluate the effects of evaporation on $\delta^{18}O_{sc}$ values and assess past aridity, but we first need to understand $\Delta'^{17}O$ variation in modern soils before using it in the geologic record.

Here we present *in situ* measurements of soil temperatures and isotopic data from modern soil waters ($\delta^{18}O_{sw}$, δD_{sw}, $\Delta'^{17}O_{sw}$) and soil carbonates ($\delta^{13}C_{sc}$, $\delta^{18}O_{sc}$, $\Delta'^{17}O_{sc}$, Δ_{47}) collected along a northwest-southeast transect across the Serengeti Ecosystem of northern Tanzania (Fig. 1). This transect adds critical data to oxygen and carbon isotopic systematics of modern soils in eastern Africa, which are understudied, despite the widespread application of paleosols carbonates as indicators of paleoenvironment and paleoclimate (e.g., Cerling et al., 2011; Levin et al., 2011; Lüdecke et al., 2018). We use these results to show how $\Delta'^{17}O$ of soil carbonates tracks local aridity in the Serengeti and demonstrate the potential for using the combination of

Δ_{47} and $\Delta'^{17}O$ measurements to place firm constraints on how soil water evaporation affects paleosol carbonate $\delta^{18}O$ records.

2. Isotope Notation

Stable isotopes of carbon and oxygen are reported using standard δ-notation,

$$\delta = \left(\frac{R_x}{R_{std}} - 1\right) 1000 \qquad (1)$$

where *R* is the ratio of the abundance of the heavy to light isotope, *x* indicates the sample and *std* is the standard.

The isotopic fractionation factor between any two substances (A and B) is defined as

$$\alpha_{A-B} = \frac{R_A}{R_B}$$

where *R* is the isotope ratio (heavy to light) of a material. The mass-dependent isotopic fractionation for $^{17}O/^{16}O$ and $^{18}O/^{16}O$ follows a power law relationship (Young et al., 2002):

$$^{17}\alpha_{A-B} = {}^{18}\alpha_{A-B}^{\theta} \qquad (2)$$

where θ is the fractionation exponent. This exponential relationship is linearized using δ′-notation,

$$\delta'_A = 1000 \ln\left(\frac{R_A}{R_{std}}\right) \qquad (3)$$

such that the isotopic composition of A and B can be expressed as

$$\delta'^{17}O = \theta * \delta'^{18}O \qquad (4)$$

(Miller, 2002). $\Delta'^{17}O$ is the deviation from this linear relationship, defined by a reference slope λ_{ref}

$$\Delta'^{17}O = \delta'^{17}O - \lambda_{ref}\delta'^{18}O \qquad (5)$$

Hydrological studies typically define λ_{ref} = 0.528 (Fig. S1A), which roughly approximates the value of θ for equilibrium fractionation in waters (Luz and Barkan, 2010). This slope also approximates the relationship between $\delta'^{18}O$ and $\delta'^{17}O$ in meteoric waters globally, although it is heavily weighted towards polar samples and few data are available from the tropics (Aron et al., in review; Luz and Barkan, 2010).

Clumped isotope thermometry uses Δ_i to represent the excess of an isotopologue, *i*, relative to the expected stochastic distribution. Calculating the temperature-dependent mass-47 anomaly (Δ_{47}) relative to the stochastic distribution is defined as:

$$\Delta_{47} = \left[\left(\frac{R^{47}}{R^{47*}} - 1\right) - \left(\frac{R^{46}}{R^{46*}} - 1\right) - \left(\frac{R^{45}}{R^{45*}} - 1\right)\right] * 1000 \qquad (6)$$

where

$$R^i = \frac{mass\ i}{mass\ 44} \qquad (7)$$

R^{i*} is similar to R^i but corresponds to the ratio of the sample with a stochastic distribution (Kelson et al., 2020; Passey et al., 2010; Wang et al., 2004).

3. Study Area

Soil samples were collected from the Serengeti Ecosystem, which is defined as the area covered by the wildebeest migration. The Serengeti straddles the Tanzania-Kenya border and covers an area ~24,000 km^2 (Reed et al., 2009). Soil maps indicate that almost all the soils contain pedogenic carbonate (de Wit, 1978; Jager, 1982). These soils cover a rainfall gradient of ~400 to 1200 mm yr^{-1} that extends from the southeast to northwest across the Serengeti (Reed et al., 2009). Seasonal variation in rainfall is primarily controlled by variations of the Intertropical Convergence Zone (ITCZ), which creates a short, warm dry season from December to February

and a longer, cooler dry season from June to October (Reed et al., 2009; Yin and Nicholson, 1998).

4. Materials and Methods

4.1. Field Methods

We sampled soils across the Serengeti in a transect from NW to SE to capture the greatest range in mean annual precipitation (MAP) amounts and evaporation conditions while limiting changes in vegetation (Fig. 1; Table 1). We collected samples from grasslands in intervals of ~25 km across the transect and additional samples from more woody environments were collected as time permitted. Eleven sites are described using standard protocols for field description and horizon designation (Soil Survey Staff, 2014) and then sampled for pedogenic carbonates and soil waters. We sampled pedogenic carbonates at depth intervals of 20 cm where present and focused on hard pedogenic carbonate nodules and coatings/pendants because they are better analogues for carbonates sampled in the rock record. In the lab, the pedogenic carbonates were cracked open and drilled or completely pulverized when the sample size was too small for the amount of carbonate needed for both triple oxygen and clumped isotope analyses (~130 mg).

We collected soil samples for cryogenic vacuum distillation of soil waters at ~20 cm depth intervals in soil pits using glass vials sealed with a rubber stopper and wrapped in parafilm. These samples represent a seasonal snapshot of soil water as they were sampled during the shorter, warmer dry season in February 2018. Water samples collected from nearby lakes, rivers, springs, and groundwater, were filtered using 0.45 µm PTFE filters in the field. All waters were treated with activated charcoal for 24 hours to remove organic contaminants in the lab (West et al., 2006).

We collected soil temperature data from four sites in the Serengeti National Park using nine HOBO 64K Pendant® temperature loggers buried at the following depths: Ndabaka (20, 80, and 150 cm depth), Musabi (40 and 140 cm depth), Kemarishe (30 and 100 cm depth), and Naabi Hill (20, 90, and 150 cm depth) (Fig. 1). These loggers have a quoted accuracy of ±0.53°C. Due to permitting issues, it was not possible to bury temperature loggers in the Ngorongoro Conservation Area, and therefore no data are available from the Malambo Road or Shifting Sands sites (Fig. 1). Data are trimmed to 2-22-2018 to 1-26-2019 with a start date 2 days after last logger was buried to allow soil temperatures to equilibrate (Table S1).

4.2. Soil Temperature Modeling

We modeled soil temperature as a function of time (t) and depth (z) using the following equation:

$$T(z,t) = T_{avg} + A_o \left[\sin\left(\omega t - \frac{z}{d}\right)\right] / e^{z/d} \quad (8)$$

where T_{avg} is average soil temperature, A_o is the amplitude of seasonal temperature variation at the soil surface, ω is the radial frequency (2π year^{-1}), z is depth from soil surface, and d is the "damping depth" which is related to the thermal properties of the soil and frequency of temperature fluctuations (Shukla, 2014). This is given by the equation:

$$d = \left(\frac{2\kappa}{C_v \omega}\right)^{1/2} \quad (9)$$

where κ is the thermal conductivity and C_v is the volumetric heat capacity (Shukla, 2014). For this model, we assigned T_{avg} as mean annual air temperature (MAAT) at the surface and calculated A_o using the average temperature of the warmest and coldest month from Fick and Hijmans (2017). We explored the effects of using the full range of values for κ and C_v, which can vary with soil texture and water content (Shukla, 2014), on damping depth and modeled temperatures but the impacts were almost imperceptible. Therefore, our calculations of damping

depth use average values of κ (1.02 W/m/°K) and C_v (2.08 J/m^3/°K) reported by Shukla (2014). Traditionally, this soil temperature model is used for environments at higher latitudes with four temperature seasons over one annual revolution (i.e., 2π year^{-1}), but equatorial Africa has only two distinct temperature peaks in a year. For this reason, we double the radial frequency (ω), which is the rate of change of phase of the sinusoidal waveform used to represent annual temperature fluctuations, to simulate two temperature peaks per year.

4.3. Stable Isotope Measurements

All stable isotope measurements were made at the University of Michigan. Water δD and $\delta^{18}O$ were analyzed on a Picarro L2130-i cavity ringdown spectrometer with an A0211 high-precision vaporizer and attached autosampler. Each sample was analyzed 10 times; we report the average of the last 5 analyses. The Picarro ChemCorrect software was used to monitor samples for organic contamination and normalized measured $\delta^{18}O$ and δD to the VSMOW-SLAP scale with USGS reference waters (USGS45, 46, 49, and 50) and four in-house liquid standards. Precision of repeat analyses of deionized water was better than 0.1‰ and 0.3‰ for $\delta^{18}O$ and δD, respectively. Soil waters were extracted using cryogenic vacuum distillation (West et al., 2006).

Carbon and oxygen stable isotope compositions ($\delta^{13}C_{sc}$ and $\delta^{18}O_{sc}$) of powdered carbonates were analyzed on a Nu Perspective isotope ratio mass spectrometer (IRMS) in the Isotopologue Paleosciences Laboratory with an online Nu Carb autosampler and digested in 100% H_3PO_4 at 90°C. Corrections are based on a two-point calibration using the NBS-18 and NBS-19 calcite standards and are reported using the standard δ-notation (Equation 1) relative to VPDB in ‰ units (Table S2 and 3). Precision (1σ, hereafter reported using ±) for the standards during the analytical interval for these unknowns was <0.02‰ for $\delta^{13}C$ and <0.05‰ for $\delta^{18}O$.

Clumped isotope analyses of carbonates (Δ_{47}) were conducted using a custom built device for the reaction of samples in 100% H_3PO_4 at 90°C and purification of the resultant CO_2 through multiple cryogenic traps and a gas chromatograph (GC) column at -20°C (Passey et al., 2010). Isotope ratios of the stable CO_2 isotopologues were then analyzed on a Nu Perspective IRMS. Δ_{47} values were normalized to the carbon dioxide equilibrium scale following Dennis et al. (2011) and Δ_{47} temperatures ($T_{\Delta47}$) were calculated using Equation 3 from Bonifacie et al. (2017) based on 2 to 5 replicates (Tables S4, S5). The Δ_{47} standard error (SE) for each sample is calculated using the SE from replicate analyses. We use the pooled standard deviation (σ_p) of secondary reference standards to document the external reproducibility of replicates using performance of ETH-1 to ETH-4, NBS-19, and three internal standards (102-GC-AZ01, GON06-OES, and Hagit Carrara), which have a σ_p of 0.019‰ for Δ_{47} (Table S6). The reconstructed oxygen isotope composition of the soil carbonate parent waters ($\delta^{18}O_{rsw}$) was calculated using $T_{\Delta47}$ and the calcite-water fractionation factor temperature equation by Kim and O'Neil (1997). The error on the $\delta^{18}O_{rsw}$ is propagated from the error associated with $T_{\Delta47}$. A few samples with lower than expected temperatures for equatorial tropical soils were treated with 3% H_2O_2 to remove organic contaminants. Treatment resulted in temperatures within error of the untreated samples (Table S5).

The $^{18}O/^{16}O$ and $^{17}O/^{16}O$ ratios of water samples were measured on O_2 generated by passing water through a 370°C cobalt (III) fluoride reactor and then analyzed using a Nu Perspective IRMS at the University of Michigan. These methods are summarized in Li et al. (2017) and have changed very little except that O_2 was previously analyzed on a Thermo 253 IRMS at Johns Hopkins University. The triple oxygen isotope composition of carbonate samples were measured using the acid digestion-reduction-fluorination method (Passey et al., 2014).

Isotopic data from analyses of both water and carbonate were normalized to the VSMOW-SLAP scale (Schoenemann et al., 2013), and results from the carbonate analyses were subjected to an additional normalization step to correct for mass dependent fractionation in $\delta^{18}O$ and $\delta^{17}O$ detailed in Section 2.3 of Passey et al. (2014). This correction does not affect $\Delta'^{17}O$ values because the fractionation effects are mass-dependent with a slope that is not resolvable from λ_{ref} = 0.528.

The precision for the triple oxygen isotope analyses of waters was determined using performance of USGS45 (n=11), USGS50 (n=6), USGS47 (n=6), and GISP (n=4). Standard deviations for $\delta'^{18}O$, $\delta'^{17}O$, and $\Delta'^{17}O$ were <0.6‰, 0.3‰, and 15 per meg, respectively. During the interval of time when these waters were analyzed, the σ_p was 0.5‰, 0.2‰, and 11 per meg for $\delta'^{18}O$, $\delta'^{17}O$, and $\Delta'^{17}O$, respectively. Carbonate precision for $\delta'^{18}O$, $\delta'^{17}O$, and $\Delta'^{17}O$ was evaluated using three standards NBS-19 (n=6), NBS-18 (n=3) and 102-GC-AZ01 (n=2; internal standard). Standard deviations for $\delta'^{18}O$, $\delta'^{17}O$, and $\Delta'^{17}O$ were <3.1‰, 1.6‰, and 4 per meg, respectively. σ_p for the carbonate standards was 2.5‰, 1.3‰, and 3 per meg for $\delta'^{18}O$, $\delta'^{17}O$, and $\Delta'^{17}O$, respectively (Table S6). Subsequent analyses have shown that the precision for these sessions is similar to the long-term, external precision of waters analyzed in the University of Michigan system, which has a pooled standard deviation of USGS reference waters of 0.3‰, 0.5‰, and 8 per meg for $\delta'^{17}O$, $\delta'^{18}O$, and $\Delta'^{17}O$, respectively (Aron et al., in review). See Tables S6-S11 for the results and normalization approach for all analyses.

5. Results

5.1. *Soil Description and Temperatures*

Eleven soils sampled for this study include Inceptisols, Mollisols, and Alfisols (Table S12, Figs. S2A-D). These USDA soil order classifications are only based on field description to summarize the dominant features of each soil and do not include any laboratory analysis as the carbonates were the focus of this study. At 9 of the 11 sites, pedogenic carbonate was identified, which ranged in morphology from hard nodules to carbonate coatings and pendants to indurated petrocalcic horizons. Representative examples of each type of soil carbonate morphology are shown in Figure S2E-I.

Results from the HOBO© temperature loggers are shown in Figure 2A and represent a 11-month long log of soil temperature variation. Maximum soil temperatures, variance, and standard deviation decrease with depth at each site and minimum temperatures increase with depth (Table 2). The mean soil temperatures of these grassland soils decrease to the southeast in the transect, similar to MAAT (Table 2; Figs. 1 and 2A) with the exception of Kemarishe, which has the highest MAST of any of the soils measured. Results from the soil temperature modeling are shown using two different depths (20 and 150 cm) from the warmest (Ndabaka) and coolest site (Naabi Hill), which had temperature logger data available for comparison (Figs. 3A-D). These results show that the soil temperature modeling generally follows the seasonal changes in air temperature, which peaks twice yearly. The amplitude of temperature variation decreases with increasing depth and temperatures at depth lag those closer to the surface.

5.2. Waters - $\delta^{18}O$, d-excess, and $\Delta'^{17}O$

$\delta^{18}O$ values range from -5.0‰ to 10.4‰ (n=64), d-excess values range from -16.3 to 58.5‰, and $\Delta'^{17}O$ values range from -24 to 25 per meg for water samples from springs, lakes, rivers, pools, and precipitation (n=45; Table S13; Figs. 4B, 4C, and 5C). Soil waters (n=16)

range from -3.8 to 5.5‰ for $\delta^{18}O$ ($\delta^{18}O_{sw}$), -31.1 to 11.6‰ for d-excess (d-excess$_{sw}$), and -13 to 63 per meg for $\Delta'^{17}O$ ($\Delta'^{17}O_{sw}$) (Figs. 4B, 4C, 5A-D).

5.3. Carbonates - $\delta^{13}C$ $\delta^{18}O$, Δ_{47}, and $\Delta'^{17}O$

We analyzed sixty-nine unique soil carbonate nodules from 9 sites (Table S2; Fig. 1) for $\delta^{13}C$ and $\delta^{18}O$ to explore isotopic variation between sites, at different depths within a single profile, and between nodules at each depth. Mean $\delta^{18}O_{sc}$ values range from -4.5‰ at Banagi to 4.3‰ at Shifting Sands, but there is no consistent trend with depth (Table S3; Fig. 6B). There is no trend across the transect, but rather a step-wise increase in $\delta^{18}O_{sc}$ at the most arid sites, Malambo Road and Shifting Sands. $\delta^{18}O_{sc}$ ranges from -0.98 to 4.3‰ at Malambo Road and Shifting Sands, whereas $\delta^{18}O_{sc}$ values from all other sites range from -4.5 to -1.5‰. $\delta^{13}C_{sc}$ values of soil carbonates range from -2.7‰ at Musabi to 1.8‰ at Shifting Sands (Table S2; Fig. 6A). The relationships between $\delta^{13}C_{sc}$ values and depth vary among the sampling sites, with some sites showing slight increases (e.g. Nyaruswiga) or decreases in $\delta^{13}C_{sc}$ values (e.g. Musabi, Ndabaka, Naabi Hill), and others not varying at all (e.g. Simba Kopjes, Naabi Hill) (Table S2; Fig 6C).

We selected a subset of these samples for Δ_{47} analysis (n=28), targeting at least one sample from each depth in a soil profile where carbonate was present. At sites where carbonate was only present at a single depth (i.e. Malambo Road, Shifting Sands, Banagi), we analyzed two different samples from that depth. $T_{\Delta47}$ from all carbonates sampled ranges from 14 to 31 °C with an average of 23 ±4 °C (Table S5; Fig. 2B). Only Ndabaka shows a trend between $T_{\Delta47}$ and soil depth, where $T_{\Delta47}$ values range from 29 ±6°C at the top of the carbonate zone (70 cm) to 19 ±3°C at the base (130 cm). We calculated $\delta^{18}O_{rsw}$ using $T_{\Delta47}$ and $\delta^{18}O_{sc}$ values and the temperature dependent fractionation factor between water and carbonate under equilibrium

conditions (Kim and O'Neil, 1997). $\delta^{18}O_{rsw}$ values range from 1.1 to 5.9‰ at the most arid sites, Malambo Road and Shifting sands and from -3.2 to 1.6‰ elsewhere. These calculations indicate that higher $\delta^{18}O_{sc}$ values at more arid sites are not produced by changes in $T_{\Delta47}$, but instead reflect higher soil water $\delta^{18}O$ values (Fig. 7A).

We prioritized $\Delta'^{17}O$ analysis of samples from sites that represented the full range of environments (from semi-arid at Malambo and Shifting Sands to dry-subhumid at Ndabaka). We analyzed samples from Simba Kopjes to represent an intermediate environment and because it has carbonate at multiple depths. The $\Delta'^{17}O$ values of soil carbonate ($\Delta'^{17}O_{sc}$) range from -162 to -106 per meg, with an average of -127 ±20 per meg (Table S5). We calculate the $\Delta'^{17}O$ of reconstructed soil water ($\Delta'^{17}O_{rsw}$) using $T_{\Delta47}$, which provides the necessary temperature information to calculate $^{18}\alpha$ ($CaCo_3$–H_2O) (Kim and O'Neil, 1997). $^{17}\alpha$ ($CaCO_3$–H_2O) is calculated using the value for $^{18}\alpha$ in the following equation:

$$\boxed{^{17}\alpha = {}^{18}\alpha^{\lambda}} \quad (10)$$

where λ is assumed to be 0.5245 (Fig. S1C; Passey et al., 2014). $\Delta'^{17}O_{rsw}$ ranges from -31 to 20 per meg, with an average of 0 ±21 per meg (Fig. S1C; Table S5).

6. Discussion

6.1. Water Isotopes

Despite a growing isotopic dataset from meteoric waters in eastern Africa (Bedaso et al., 2020; Levin et al., 2009; Odada, 2001; Otte et al., 2017; Rozanski et al., 1996), we are not aware of any $\delta^{18}O$ and δD data from meteoric waters for the Serengeti Ecosystem. The closest systematic rainfall collections are from the Global Network for Isotopes in Precipitation (GNIP) station in Nairobi, >200 km to the northeast, and on the slopes of Mt. Kilimanjaro, >250 km to

307 the southeast (Otte et al., 2017; Rozanski et al., 1996). The new $\delta^{18}O$ and δD values of the waters
308 from the Serengeti (Table S13; Figs. 4B and C) fall in the range of interpolated values from the
309 GNIP dataset (Fig. 4A; Bowen, 2020; Bowen and Revenaugh, 2003). $\Delta'^{17}O$ data from African
310 waters are very limited, but surface and tap water data from Mpala, Kenya range from -16 to 24
311 per meg (Li et al. 2017) and range from -18 to 26 per meg for monsoonal precipitation from
312 Niger (Landais et al., 2010), similar to $\Delta'^{17}O$ values of -25 to 23 per meg measured for this study
313 (Fig. 5A and C).

314 Grouping the data by water type, we observe that $\delta^{18}O$ and δD values of groundwater,
315 precipitation and springs plot on or close to the global, regional and local meteoric water lines
316 (Fig. 4B; Dansgaard, 1964; Otte et al., 2017; Rozanski et al., 1996), whereas pools, rivers, and
317 lakes from the Serengeti plot to the right of these meteoric water lines. These surface waters have
318 higher $\delta^{18}O$ values (2.8 ±3.9‰), lower d-excess values (3.6 ±9.9‰), and lower $\Delta'^{17}O$ values (-3
319 ±13 per meg) than isotopic values of groundwater, precipitation, and springs (-2.8 ±2.2‰; 16.8
320 ±11.0‰, 12 ±10 per meg) (Figs. 4B, 4C, 5A, and 5C). This distinction indicates the role of
321 evaporation in modifying the isotopic composition of Serengeti surface waters. The waters were
322 collected in February 2018 during the shorter but hotter dry season (December to February),
323 when maximum evaporative water loss may be expected.

324 Soil waters are isotopically distinct from both surface waters and precipitation/spring
325 waters, yielding average $\delta^{18}O$, d-excess and $\Delta'^{17}O$ values of -0.9 ±2.3‰, -4.2 ±12.4‰, and 14
326 ±18 per meg (Figs. 4B, 4C, 5B and D), respectively. Like surface waters, soil waters plot to the
327 right of the meteoric water line and yield relatively low d-excess and $\Delta'^{17}O$ values, indicating the
328 influence of evaporation. The effects evaporation on soil water has been observed in $\delta^{18}O$ and
329 δD values in modern soils (Hsieh et al., 1998) and experimentally demonstrated and modeled in

the laboratory (Allison et al., 1983; Barnes and Allison, 1983), though not previously demonstrated for $\Delta'^{17}O$. However, lower $\delta^{18}O$ values in soil waters than surface waters suggest recharge at different times. Shifting Sands and Malambo Road were collected after a recent storm, which is observed in the isotopic data and suggests that recent rains disproportionally contributed to the soil water pool and are not representative of annually integrated soil water. The $\delta^{18}O_{sw}$ values are ~2 to 4‰ lower at 20 cm than samples at 40 cm and the d-excess$_{sw}$ and $\Delta'^{17}O_{sw}$ are higher at the surface (~20 to 30‰ and 30 to 40 per meg, respectively) than those at depth (Figs. S3A, C, and E).

6.2. Measured, Modeled, and Clumped Isotope Soil Temperatures

Soil temperature monitoring is an important component to understand the conditions of soil carbonate formation in the Serengeti and to interpret our $T_{\Delta47}$ results. Here we compare our 11-month logs of soil temperature to existing but limited air temperature and soil temperature from the Serengeti. Mean Annual Soil Temperatures (MAST) for all depths range from 23 to 26°C for this study (Table 2). This is similar to existing records of MAAT (21°C) and MAST (25°C, 50 cm depth) at Serengeti National Park, collected in 1975-1976 from the Serengeti Research Institute located near the center of the Serengeti National Park (Jager, 1982). This is also similar to MAAT values produced from spatial interpolations (Fick and Hijmans (2017), which range from 19 to 22°C.

Our temperature monitoring in the Serengeti shows that soil temperature varies by vegetation type such that grassland soils (Ndabaka, Musabi, and Naabi Hill) are cooler on average than the grassed woodland soil (Kemarishe). For example, mean temperatures from the lowest depths of each soil are statistically lower for Ndabaka (26.40 ± 0.35°C), Musabi (25.90 ± 0.58°C), and Naabi Hill (23.78 ±0.44°C) than those from Kemarishe (26.73 ±0.78°C) (Tables 2

353 and S14; Fig. 2A). The mean temperatures from Kemarishe are the warmest among all the sites
354 and have the highest minimum temperatures and warmest maximum temperatures although
355 shaded woodlands are typically cooler than grasslands (Cerling et al., 2011). This may be due to
356 a local climate anomaly, water use differences between these sites, or a product of the
357 distribution of trees and shrubs at Kemarishe, which are not densely packed in a grassed
358 woodland.

359 Modeling of Serengeti soil temperatures indicates a 2 to 3°C range over the year, which
360 is similar to measured temperatures that vary from ~1 to 2.5°C at 150 cm depth (Table 2).
361 Limited variation in soil temperature is expected at the equator where variations in MAAT are
362 limited to ±4°C in the Lake Victoria Basin, which includes the Serengeti (Yin and Nicholson,
363 1998). Despite the similarity in amplitude, we note that modeled soil temperatures are 3 to 4°C
364 cooler than observed temperatures because this simple model does not account for ground
365 heating by incident solar radiation, which is significant in grassland soils that receive direct
366 sunlight (Fig. 2A; Quade et al., 2013) like the grassland soils in this study. Ground air
367 temperature increases with observed solar radiation by 1.21 K/100 W m^{-2} (Bartlett et al., 2006).
368 The Lake Victoria Basin receives on average 412 W m^{-2} of incident solar radiation (Yin and
369 Nicholson, 1998), which may increase temperature by up to 5°C in the Serengeti and may
370 explain the discrepancy of 3 to 4 °C between the modeled and measured soil temperatures (Figs.
371 3E and F). When we account for ground heating and add 5°C to our model results, the range of
372 modeled temperatures overlaps with most of the $T_{\Delta 47}$ results and the range of measured soil
373 temperatures (Fig. 2B). The measured soil temperatures and modeling show very little
374 seasonality and likely explains why we observe little variation in $T_{\Delta 47}$ by depth among

carbonates for these same soils, with the exception of Ndabaka, where temperature decreases from 29 to 19 °C from 70 to 130 cm depth.

Overall, $T_{\Delta47}$ of soil carbonates from the Serengeti range from 14 to 29°C with an average of 23 ±4°C and plot within the range of soil temperature measured over the 11-month monitoring campaign (Fig. 2B). These Serengeti temperatures are similar to single $T_{\Delta47}$ measurement of 18.8 ±1.6°C from nearby Masai Mara Park, ~100 km north of the Serengeti transect in Kenya (Passey et al., 2010). Data available from other parts of eastern Africa are significantly warmer than the Serengeti by 5 to 10°C. Modern soil temperatures from the Turkana region in northern Kenya have a mean of 35°C and maximum of 38°C at 50 cm depth (Passey et al., 2010), which is >10°C warmer than any soils from the Serengeti. Soil temperatures from the Afar region of Ethiopia are also warmer with a mean of 28°C and maximum temperature of 29°C at ~50 cm depth for both grassland and wooded soils (Passey et al., 2010). $T_{\Delta47}$ values reconstructed from soil carbonates in the Afar range from 25 to 40°C and are consistent with the range of measured soil temperatures (Passey et al., 2010). Further south in the Karonga Basin near Lake Malawi, soil temperatures at 40 cm depth range from a mean of 27 ±2.1°C in partial shade to a mean of 31 ±3.2°C in full sun (Lüdecke et al., 2018).

Soil carbonates can form in different periods throughout the year but primarily form during the warm, dry season (Breecker et al., 2009; Kelson et al., 2020; Passey et al., 2010; Quade et al., 2013), and for this reason most Δ_{47} studies of modern soil carbonates identify a warm season bias in $T_{\Delta47}$ (Kelson et al., 2020, and references therein). However, elevation likely explains much of the difference in mean soil temperature between Turkana, Afar, and Karonga (400 to 500 meters above sea level) and the Serengeti (1100 to 1600 masl). The lapse rate in eastern Africa is -5.8°C/km (Loomis et al., 2017), and so the rest of this 5 to 10°C discrepancy

between the Serengeti and Turkana, Afar, and Karonga can likely be explained by a combination of aridity and seasonality of temperature. The lowest measured soil temperatures in eastern Africa occur in the Serengeti with the highest elevation and a MAP of 400 to 850 mm yr^{-1}. The warmest temperatures occur in the Afar and Turkana at low elevations and low MAP (300 to 400 mm yr^{-1}). Karonga is at lower elevation but higher MAP (~1111 mm yr^{-1}) falls in between (Fick and Hijmans, 2017).

6.3. Carbonate Isotopes and Vegetation Relationships

Despite the abundance of research on paleosol carbonates in Africa in conjunction with paleoanthropological research (e.g., Cerling et al., 2011; Levin et al., 2011; Lüdecke et al., 2018), there are few studies of modern African pedogenic carbonates. In Figure 6A, the gray dots show all known modern $\delta^{13}C_{sc}$ and $\delta^{18}O_{sc}$ data available from the literature for Africa from Libya, Morocco, and South Africa (n=51) and the black dots represent samples in eastern Africa from Kenya, Tanzania, and Ethiopia (n=16) (Cerling and Quade, 1980; Passey et al., 2010; Salomons et al., 1978).

The carbon isotope data from the Serengeti soils plot among the highest $\delta^{13}C_{sc}$ values relative to other African modern soils and correspond to grassland vegetation with the exception of three samples from Musabi. All sites were mapped as grassland vegetation with the exception of Makoma (shrubland) and Kemarishe (woodland) (Reed et al., 2009), which did not have pedogenic carbonate identified in the soil, and therefore no comparisons could be made. The three exceptions from Musabi are classified as wooded grasslands, but the average $\delta^{13}C_{sc}$ for Musabi is -0.3 ±1.4‰ (Table S3). This suggests that $\delta^{13}C_{sc}$ faithfully represents the vegetation of the environments in which they form. In addition to the expected relationship with vegetation, $\delta^{13}C_{sc}$ values should increase at the surface (<40 cm depth) due to interaction with an enriched

atmosphere and $\delta^{18}O_{sc}$ should increase towards the surface due to evaporative enrichment and (Figs. 6B and C; Breecker et al., 2009). However, we did not observe these expected relationships because there was no pedogenic carbonate > 40 cm at these sites.

6.4. Relationship between $\Delta'^{17}O_{sc}$ and Aridity

The combination of $\delta^{18}O_{sc}$ and Δ_{47} data from the Serengeti indicate that $\delta^{18}O_{rsw}$ values for some sites are considerably higher (8‰) than $\delta^{18}O$ values of local unevaporated waters (precipitation, springs, groundwater) and indicate that these carbonates formed from waters that experienced considerable evaporation (Fig. 7A). This is consistent with studies from other arid regions, where $\delta^{18}O_{rsw}$ values are significantly higher than local $\delta^{18}O_{mw}$ values and attributed to evaporation (Quade et al., 2007). In the Serengeti, enriched $\delta^{18}O_{rsw}$ values are only observed at Malambo Road and Shifting Sands. Other sites plot within ±2‰ of the expected $\delta^{18}O_{mw}$ with the exception of one sample from Simba Kopjes (Fig. 7A). There are no clear distinctions in measured soil temperatures, $T_{\Delta47}$, vegetation, or soil texture among these sites to explain these elevated $\delta^{18}O_{rsw}$ values (Tables 1, S1, S5, and S12). The main distinguishing feature is the climate of the sites.

We differentiate the climate of these sites in terms of aridity, using the aridity index (AI = MAP/PET), where there are five broad climate classes: hyper arid, arid, semi-arid, dry sub-humid, and humid (Middleton and Thomas, 1997). AI values for Malambo Road and Shifting Sands plot as semi-arid (0.33-0.38), whereas the remaining sites yield higher AI values (0.51-0.55) that cluster in the dry sub-humid category (Table 1; Fig. 7C). Another common method of differentiating aridity uses water deficit (WD = PET-MAP) where high values indicate a greater water deficit. Malambo Road and Shifting Sands similarly have a high WD of 963 to 1084 mm yr^{-1} and all other sites range from 717 to 829 mm yr^{-1} (Table 1: Fig. 7D).

The $\Delta'^{17}O$ and $\delta'^{18}O$ values of soil carbonates in the Serengeti track aridity. $\Delta'^{17}O_{rsw}$ values are >50 per meg lower at semi-arid sites (Malambo Road, Shifting Sands) than at dry sub-humid sites (Simba Kopjes, Ndabaka, and Banagi; Fig. 7C). We also observe a sharp increase in $\delta'^{18}O_{rsw}$ values from -4.4 to 6.1‰ with increased aridity (Fig. 7A and Table S5). A single soil carbonate from Ndabaka (AI = 0.55), with a $\Delta'^{17}O_{rsw}$ value of -11 per meg, is an exception to this trend. It is the shallowest sample from this profile (70 cm depth) and the combination of lower $\Delta'^{17}O_{rsw}$ values and higher $\delta'^{18}O_{rsw}$ values (Fig. 7B) likely reflect increased evaporation of soil water closer to the surface (Fig. S4).

These data match our expectations for decreased $\Delta'^{17}O$ and increased $\delta'^{18}O$ values in more arid sites where evaporation drives isotopic fractionation of soil water (Fig S1B). The influence of evaporation on triple oxygen isotope composition of waters is well documented in lakes and ponds, which document clear and predictable trends in $\delta'^{18}O$ and $\Delta'^{17}O$ values of surface waters that follow distinct evaporation slopes (λ) that range from 0.518 to 0.528 and reflect conditions of evaporation in surface waters (e.g., Gázquez et al., 2018; Passey and Ji, 2019; Surma et al., 2018). We plot the $\delta'^{18}O_{rsw}$ and $\Delta'^{17}O_{rsw}$ values from the Serengeti soils in the context of these evaporation slopes. Assuming that unevaporated soil water is has an isotopic composition similar to spring water ($\delta'^{18}O$ = -5‰, $\Delta'^{17}O$ = 20 per meg; Table S13), evaporation slopes of 0.518 – 0.524, that are typical of lakes, capture most of the observed isotopic variation in the Serengeti carbonates (Fig. 7B).

The triple oxygen isotopic composition of the dry season soil waters collected from the Serengeti exhibit different trends than the soil waters reconstructed from soil carbonates (Fig. 5D). $\Delta'^{17}O_{sw}$ and $\Delta'^{17}O_{rsw}$ are indistinct from each other at Ndabaka. At Simba Kopjes, $\Delta'^{17}O_{rsw}$ are largely invariant (Fig. 7B), but $\Delta'^{17}O_{sw}$ values follow evaporation slopes and are up to 18 per

meg lower than $\Delta'^{17}O_{rsw}$ values (Fig. 5D). In contrast, at Malambo Road and Shifting Sands, $\Delta'^{17}O_{rsw}$ values are of >50 per meg more negative than $\Delta'^{17}O_{sw}$ values (Figs. 5D and 7B). As discussed in Section 6.1, isolated collections of soil waters may represent a snapshot of conditions and may be strongly influenced by a recent wetting or drying event. In contrast, the isotopic composition of the soil waters reconstructed from soil carbonates represent average soil conditions over the duration of carbonate formation.

The clear association of lower $\Delta'^{17}O_{rsw}$ values at more arid sites (with lower AI and higher WD) indicates the strong influence of evaporation on the oxygen isotopic composition on soil carbonates in the Serengeti (Figs. 7C, 7D). The observed spatial variability in this transect is important for building a framework for interpreting similar data from the geologic record where we can infer trends through time. Using a suite of measurements including $\delta^{18}O_{sc}$, Δ_{47}, and $\Delta'^{17}O_{sc}$, gives the ability to reconstruct both soil temperatures and $\delta^{18}O_{rsw}$ values which can then be used in combination with $\Delta'^{17}O_{rsw}$ to evaluate the role of evaporation in driving variation in $\delta^{18}O_{sc.}$ This is an advance over current approaches in which $\delta^{18}O_{rsw}$ values are determined from $\delta^{18}O_{sc}$ and $T_{\Delta47}$ measurements (or assumed soil temperature) and are difficult to interpret because the soil water evaporation is unconstrained. For example, there are large differences in the trends of $\delta^{18}O_{sc}$ values over the last 4 Ma in eastern Africa; $\delta^{18}O_{sc}$ values remains constant over the last 4 Ma in the Afar region of Ethiopia but increase by up to 10‰ in the Omo-Turkana Basin in northern Kenya and southern Ethiopia (Levin et al., 2011). We cannot presently evaluate the role of soil water evaporation on these $\delta^{18}O_{sc}$ records, but $\Delta'^{17}O_{sc}$ measurements could provide this constraint.

Although $\Delta'^{17}O_{sc}$ is directly sensitive to evaporation, it may also provide insights into aridity. Aridity is a key variable to understanding the ecosystem pressures on organisms when

reconstructing past environments, but it is hard to capture in a proxy as it results from the interplay of rainfall amounts, temperature, and evaporative water loss. The Serengeti soil carbonate data show that $\Delta'^{17}O_{rsw}$ values track aridity, where $\Delta'^{17}O_{rsw}$ values decrease by ~ 50 per meg between semi-arid and dry sub-humid environments, indicating that there may be a threshold for soil water evaporation between these climate classes (Fig. 7C). We observe a similar shift in $\Delta'^{17}O_{rsw}$ values when plotted against the water deficit for this region with the most negative $\Delta'^{17}O_{rsw}$ values at sites with the highest water deficit (Fig. 7D). These data hint at the value of using $\Delta'^{17}O_{rsw}$ values to track aridity in the geologic record, but it needs to be fully tested in other geographic regions, in additional soil types, ecosystems and in a broader range of climate classes (hyper-arid, arid, and humid).

7. Conclusions

The isotopic composition of soil carbonates is a widely used tool for tracking vegetation, temperature, and climate in the geologic record. Our study of soil carbonates sampled along an aridity gradient in the Serengeti, Tanzania, expands the utility of this tool by providing 1) new data on landscape-scale variation in $\delta^{13}C$, $\delta^{18}O$ and Δ_{47} values from modern soils in Africa, where there are few isotopic datasets and 2) the first detailed look at the distribution of $\Delta'^{17}O$ values in modern soil carbonates and soil waters and how they vary with aridity. We find that the Serengeti $\delta^{13}C_{sc}$ values indicate 'grassland' within the framework of the fractional woody cover proxy (Cerling et al., 2011), which is consistent with mapped vegetation. The $\delta^{18}O_{sc}$ values of the Serengeti soils exhibit a large range (-5 to 4‰), with the highest $\delta^{18}O_{sc}$ values at the most arid sites, indicating the importance of increased soil water evaporation on $\delta^{18}O_{sc}$ values in arid

settings. This trend holds for $\delta^{18}O_{rsw}$ values, which we determine from Δ_{47} temperatures values to constrain soil formation temperatures.

Our Δ_{47} data indicate that these carbonates record temperatures (ranging from 14 to 29°C with an average of 23 ±4°C) that span the range of MAAT and MAST and the soil temperatures measured over an 11-month monitoring interval. The *in situ* measurement of soil temperatures and soil modeling indicate that ground heating may increase soil temperature by up to 5°C above MAAT. We observe very little $T_{\Delta47}$ variation with depth, likely because there is so little annual temperature variation near the equator. Although there are few other $T_{\Delta47}$ datasets from modern soil carbonates in Africa, the $T_{\Delta47}$ from the Serengeti are similar to carbonate sampled nearby at Masai Mara Kenya (18.8 ±1.6°C), but cooler than the $T_{\Delta47}$ values from modern soil carbonates in the Afar region of Ethiopia (25–40°C), which is also reflected in measured soil temperatures. Cooler soil temperatures in the Serengeti is likely due a combination of its higher elevation, reduced temperature seasonality in the tropics, and higher precipitation.

Finally, our work provides the first systematic view of the distribution of $\Delta'^{17}O$ values in soil carbonates. We observe that $\Delta'^{17}O_{rsw}$ values decrease by >50 per meg and $\delta^{18}O_{rsw}$ values increase by >5‰ from the dry sub-humid sites (Ndabaka, Simba Kopjes, and Banagi) to the semi-arid sites (Shifting Sands and Malambo Road), which likely reflects increased soil water evaporation at the semi-arid sites. Differences in $\Delta'^{17}O_{rsw}$ and $\delta^{18}O_{rsw}$ between sampling sites along the Serengeti transect are far greater than the typical measurement error and show that a combination of $\delta^{18}O$, Δ_{47}, and $\Delta'^{17}O$ measurements in soil carbonates can be used to detect spatial differences in aridity in modern landscapes. Finally, the ability to constrain the influence of both temperature and evaporation on $\delta^{18}O_{sc}$ values will transform interpretations of long-term

records of $\delta^{18}O_{rsw}$ and allow for direct comparisons between different sites, environments, and time periods, in a way that has previously not been possible.

Acknowledgements

This research was conducted under COSTECH Permit #2018-39-NA-2018-17, TANAPA Research Permit #: TNP/HQ/C.10/13, and TAWIRI Permit #: TWRI/RS-342/2016/116. This work was supported by the National Science Foundation [EAR-PF grant #1725621] and the University of Michigan Earth and Environmental Sciences Department. The authors would like to thank Joseph Masoy, Honest Ndoro, and Audax Mabulla for their help with fieldwork and permitting, which made this research possible. The authors would also like to thank Chris Poulsen for the use of the laboratory and Picarro L2130-i and Ryan Horwitz for assistance with analyses. Finally, the authors would like to thank Ian Z. Winklestern, who's discussions and assistance in the laboratory were invaluable to the success of this research. All data are available in the supporting information.

References

Allison, G.B., Barnes, C.J., Hughes, M.W., 1983. The distribution of deuterium and 18O in dry soils 2. Experimental. J. Hydrol. 64, 377–397. https://doi.org/10.1016/0022-1694(83)90078-1

Aron, P.G., Levin, N.E., Beverly, E.J., Huth, T.E., Passey, B.H., Pelletier, E.M., Poulsen, C.J., Winkelstern, I.Z., Yarian, D.A., in review. Triple oxygen isotopes in the water cycle. Chem. Geol.

Bao, H., Cao, X., Hayles, J.A., 2016. Triple Oxygen Isotopes: Fundamental Relationships and Applications. Annu. Rev. Earth Planet. Sci 44, 463–92. https://doi.org/10.1146/annurev-earth-060115-012340

Barnes, C.J., Allison, G.B., 1983. The distribution of deuterium and O18 in dry soils 1. Theory. J. H 60, 141–156.

Bartlett, M.G., Chapman, D.S., Harris, R.N., 2006. A Decade of Ground – Air Temperature Tracking at Emigrant Pass Observatory, Utah. J. Clim. 19, 3722–3731.

Bedaso, Z.K., DeLuca, N.M., Levin, N.E., Zaitchik, B.F., Waugh, D.W., Wu, S.Y., Harman, C.J., Shanko, D., 2020. Spatial and temporal variation in the isotopic composition of Ethiopian precipitation. J. Hydrol. 585, 124364. https://doi.org/10.1016/j.jhydrol.2019.124364

Bonifacie, M., Calmels, D., Eiler, J.M., Horita, J., Chaduteau, C., Vasconcelos, C., Agrinier, P., Katz, A., Passey, B.H., Ferry, J.M., Bourrand, J.J., 2017. Calibration of the dolomite clumped isotope thermometer from 25 to 350 °C, and implications for a universal calibration for all (Ca, Mg, Fe)CO3carbonates. Geochim. Cosmochim. Acta 200, 255–279. https://doi.org/10.1016/j.gca.2016.11.028

Bowen, G.J., 2020. Gridded maps of the isotopic composition of meteoric waters [WWW Document]. URL http://www.waterisotopes.org

Bowen, G.J., Revenaugh, J., 2003. Interpolating the isotopic composition of modern meteoric precipitation. Water Resour. Res. 39, 1–13. https://doi.org/10.1029/2003WR002086

Breecker, D.O., Sharp, Z.D., McFadden, L.D., 2009. Seasonal bias in the formation and stable isotopic composition of pedogenic carbonate in modern soils from central New Mexico, USA. Bull. Geol. Soc. Am. 121, 630–640. https://doi.org/10.1130/B26413.1

Cerling, T.E., Quade, J., 1980. Stable carbon and oxygen isotopes in soil carbonates. Geophys. Monogr. 78, 217–231.

Cerling, T.E., Wynn, J.G., Andanje, S. a, Bird, M.I., Korir, D.K., Levin, N.E., Mace, W., Macharia, A.N., Quade, J., Remien, C.H., 2011. Woody cover and hominin environments in the past 6 million years. Nature 476, 51–56. https://doi.org/10.1038/nature10306

Dansgaard, W., 1964. Stable isotopes in precipitation. Tellus 16, 436–468.

de Wit, H.A., 1978. Soils and Grassland Types of the Serengeti Plain (Tanzania): Their distributions and interrelations. Wageningen.

Dennis, K.J., Affek, H.P., Passey, B.H., Schrag, D.P., Eiler, J.M., 2011. Defining an absolute reference frame for “clumped” isotope studies of CO2. Geochim. Cosmochim. Acta 75, 7117–7131. https://doi.org/10.1016/j.gca.2011.09.025

Fick, S.E., Hijmans, R.J., 2017. WorldClim 2: new 1-km spatial resolution climate surfaces for global land areas. Int. J. Climatol. 37, 4302–4315. https://doi.org/10.1002/joc.5086

Garzione, C.N., Hoke, G.D., Libarkin, J.C., Withers, S., MacFadden, B., Eiler, J., Ghosh, P., Mulch, A., 2008. Rise of the Andes. Science (80-.). 320, 1304–1307. https://doi.org/10.1126/science.1148615

612 Gázquez, F., Morellón, M., Bauska, T., Herwartz, D., Surma, J., Moreno, A., Staubwasser, M.,
613 Valero-Garcés, B., Delgado-Huertas, A., Hodell, D.A., 2018. Triple oxygen and hydrogen
614 isotopes of gypsum hydration water for quantitative paleo-humidity reconstruction. Earth
615 Planet. Sci. Lett. 481, 177–188. https://doi.org/10.1016/j.epsl.2017.10.020
616 Hsieh, J.C.C., Chadwick, O.A., Kelly, E.F., Savin, S.M., 1998. Oxygen isotopic composition of
617 soil water: Quantifying evaporation and transpiration. Geoderma 82, 269–293.
618 https://doi.org/10.1016/S0016-7061(97)00105-5
619 Jager, T.J., 1982. Soils of the Serengeti Woodlands.
620 Kelson, J.R., Huntington, K.W., Breecker, D.O., Burgener, L.K., Gallagher, T.M., Hoke, G.D.,
621 Petersen, S. V., 2020. A proxy for all seasons? A synthesis of clumped isotope data from
622 Holocene soil carbonates. Quat. Sci. Rev. 234, 106259.
623 https://doi.org/10.1016/j.quascirev.2020.106259
624 Kim, S.-T., O'Neil, J.R., 1997. Equilibrium and nonequilibrium oxygen isotope effects in
625 synthetic carbonates. Geochim. Cosmochim. Acta 61, 3461–3475.
626 https://doi.org/10.1016/S0016-7037(97)00169-5
627 Landais, A., Risi, C., Bony, S., Vimeux, F., Descroix, L., Falourd, S., Bouygues, A., 2010.
628 Combined measurements of 17Oexcess and d-excess in African monsoon precipitation:
629 Implications for evaluating convective parameterizations. Earth Planet. Sci. Lett. 298, 104–
630 112. https://doi.org/10.1016/j.epsl.2010.07.033
631 Levin, N., Brown, F.H., Behrensmeyer, A.K., Bobe, R., Cerling, T.E., 2011. Paleosol carbonates
632 from the Omo Group: Isotopic records of local and regional environmental change in East
633 Africa. Palaeogeogr. Palaeoclimatol. Palaeoecol. 307, 75–89.
634 Levin, N.E., Zipser, E.J., Ceding, T.E., 2009. Isotopic composition of waters from Ethiopia and
635 Kenya: Insights into moisture sources for eastern Africa. J. Geophys. Res. Atmos. 114, 1–
636 13. https://doi.org/10.1029/2009JD012166
637 Li, S., Levin, N.E., Soderberg, K., Dennis, K.J., Caylor, K.K., 2017. Triple oxygen isotope
638 composition of leaf waters in Mpala, central Kenya. Earth Planet. Sci. Lett. 468, 38–50.
639 https://doi.org/10.1016/j.epsl.2017.02.015
640 Loomis, S.E., Russell, J.M., Verschuren, D., Morrill, C., De Cort, G., Sinninghe Damsté, J.S.,
641 Olago, D., Eggermont, H., Alayne Street-Perrott, F., Kelly, M.A., 2017. The tropical lapse
642 rate steepened during the Last Glacial Maximum. Sci. Adv. 3, 1–7.
643 https://doi.org/10.1126/sciadv.1600815
644 Lüdecke, T., Kullmer, O., Wacker, U., Sandrock, O., Fiebig, J., Schrenk, F., Mulch, A., 2018.
645 Dietary versatility of Early Pleistocene hominins. Proc. Natl. Acad. Sci. 201809439.
646 https://doi.org/10.1073/pnas.1809439115
647 Luz, B., Barkan, E., 2010. Variations of 17O/16O and 18O/16O in meteoric waters. Geochim.
648 Cosmochim. Acta 74, 6276–6286. https://doi.org/10.1016/j.gca.2010.08.016
649 Middleton, N., Thomas, D. (Eds.), 1997. World Atlas of Desertification, 2nd ed. Hodder Arnold,
650 London.
651 Miller, M.F., 2002. Isotopic fractionation and the quantification of 17O anomalies in the oxygen
652 three-isotope system: an appraisal and geochemical significance. Geochim. Cosmochim.
653 Acta 66, 1881–1889.
654 Odada, E.O., 2001. Stable isotopic composition of East African lake waters (No. IAEA-
655 TECDOC--1206).
656 Otte, I., Detsch, F., Gütlein, A., Scholl, M., Kiese, R., Appelhans, T., Nauss, T., 2017.
657 Seasonality of stable isotope composition of atmospheric water input at the southern slopes

of Mt. Kilimanjaro, Tanzania. Hydrol. Process. 31, 3932–3947. https://doi.org/10.1002/hyp.11311
Passey, B.H., Hu, H., Ji, H., Montanari, S., Li, S., Henkes, G.A., Levin, N.E., 2014. Triple oxygen isotopes in biogenic and sedimentary carbonates. Geochim. Cosmochim. Acta 141, 1–25. https://doi.org/10.1016/j.gca.2014.06.006
Passey, B.H., Ji, H., 2019. Triple oxygen isotope signatures of evaporation in lake waters and carbonates: A case study from the western United States. Earth Planet. Sci. Lett. 518, 1–12. https://doi.org/10.1016/j.epsl.2019.04.026
Passey, B.H., Levin, N.E., Cerling, T.E., Brown, F.H., Eiler, J.M., Turekian, K.K., 2010. High-temperature environments of human evolution in East Africa based on bond ordering in paleosol carbonates. Proc. Natl. Acad. Sci. U. S. A. 107, 1–5. https://doi.org/10.1073/pnas.1001824107
Quade, J., Eiler, J., Daëron, M., Achyuthan, H., 2013. The clumped isotope geothermometer in soil and paleosol carbonate. Geochim. Cosmochim. Acta 105, 92–107. https://doi.org/10.1016/j.gca.2012.11.031
Quade, J., Rech, J., Latorre, C., Betancourt, J., Gleeson, E., Kalin, M., 2007. Soils at the hyperarid margin: The isotopic composition of soil carbonate from the Atacama Desert, Northern Chile. Geochim. Cosmochim. Acta 71, 3772–3795. https://doi.org/10.1016/j.gca.2007.02.016
Rech, J.A., Currie, B.S., Jordan, T.E., Riquelme, R., Lehmann, S.B., Kirk-Lawlor, N.E., Li, S., Gooley, J.T., 2019. Massive middle Miocene gypsic paleosols in the Atacama Desert and the formation of the Central Andean rain-shadow. Earth Planet. Sci. Lett. 506, 184–194. https://doi.org/10.1016/j.epsl.2018.10.040
Reed, D.N., Anderson, T.M., Dempewolf, J., Metzger, K., Serneels, S., 2009. The spatial distribution of vegetation types in the Serengeti ecosystem: The influence of rainfall and topographic relief on vegetation patch characteristics. J. Biogeogr. 36, 770–782. https://doi.org/10.1111/j.1365-2699.2008.02017.x
Rozanski, K., Araguas-Araguas, L., Gonfiantini, R., 1996. Isotope patterns of precipitation in the East African region, in: The Limnology, Climatology and Paleoclimatology of the East African Lakes. pp. 79–93.
Salomons, W., Goudie, A., Mook, W.G., 1978. Isotopic Composition of Calcrete Deposits from Europe, Africa and India. Earth Surf. Process. 3, 43–57.
Schoenemann, S.W., Schauer, A.J., Steig, E.J., 2013. Measurement of SLAP2 and GISP d17O and proposed VSMOW-SLAP normalization for d17O and 17Oexcess. Rapid Commun. Mass Spectrom. 27, 582–590. https://doi.org/10.1002/rcm.6486
Shukla, M.K., 2014. Soil Physics: An Introduction. Taylor& Francis Group, Boca Raton, FL.
Soil Survey Staff, 2014. Illustrated Guide to Soil Taxonomy, 1.0. ed. USDA NRCS, Licoln Nebraska.
Surma, J., Assonov, S., Herwartz, D., Voigt, C., Staubwasser, M., 2018. The evolution of 17O-excess in surface water of the arid environment during recharge and evaporation. Sci. Rep. 8, 4972. https://doi.org/10.1038/s41598-018-23151-6
Wang, Z., Schauble, E.A., Eiler, J.M., 2004. Equilibrium thermodynamics of multiply substituted isotopologues of molecular gases. Geochim. Cosmochim. Acta 68, 4779–4797. https://doi.org/10.1016/j.gca.2004.05.039
West, A.G., Patrickson, S.J., Ehleringer, J.R., 2006. Water extraction times for plant and soil materials used in stable isotope analysis. Rapid Commun. Mass Spectrom. 20, 1317–1321.

https://doi.org/10.1002/rcm.2456
Yin, X., Nicholson, S.E., 1998. The water balance of Lake Victoria. Hydrol. Sci. J.
Young, E.D., Galy, A., Nagahara, H., 2002. Kinetic and equilibrium mass-dependant isotope fractionation laws in nature and their geochemical and cosmochemical significance. Geochim. Cosmochim. Acta 66, 1095–1104. https://doi.org/10.1016/S0016-7037(01)00832-8

Figures

Figure 1. Location map of the study area. (a) Location of the Serengeti in Africa and the position of important climatological features: the intertropical convergence zone (ITCZ) during June, July, August (JJA) and December, January, February (DJF). (b) Location of parks where work was conducted in the Serengeti-Masai Mara Ecosystem outlined in gray over a map of the Aridity Index (MAP/PET) for northern Tanzania and southern Kenya. The locations of water sample collection sites and soil profiles are also indicated. The warmer to cooler colors of the soil profiles sites across the transect are consistent throughout Figures 3-5.

Figure 2. (a) Measured soil temperatures are plotted and smoothed to a daily average over an 11 month period and are contrasted with monthly average air temperature from Fick and Hijmans (2017). Color scheme is consistent with Figure 1. (b) Plot of $T_{\Delta 47}$ versus depth. The gray box indicates the range of measured soil temperatures from all sites and all depths. The is the range of modeled soil temperature +5°C to account for ground heating due to incident solar radiation. See Section 6.2 and Fig. 3 for explanation. Errors bars for Δ_{47} use the propagated SE of ± 0.015‰.

Figure 3. (a-d) Comparison of measured soil temperature, monthly average air temperature, and modeled soil temperature from Ndabaka in the northwest and Naabi Hill in the southeast. (a) Ndabaka site at 20 cm depth (b) Naabi Hill at 20 cm depth (c) Ndabaka at 150 cm depth (d) Naabi Hill at 150 cm depth (e-f) Results from the modeling of Ndabaka and Naabi Hill plotted with depth. The MAAT is shown by the black dashed line and MAST indicated by the solid black line. (e) The range of modeled temperatures are plotted in light blue and the range of measured values at 150 cm depth are plotted in dark blue. (e) The range of modeled temperatures are plotted in light orange and the range of measured values at 150 cm depth are plotted in dark orange. Note the +5°C which illustrates the effect of ground heating due to incident solar radiation, which is not included in this simple model, but can have a significant effect on soil temperatures (see text for additional discussion).

Figure 4. (a) Monthly and mean values for precipitation, $\delta^{18}O$ and δD from the Online Isotopes in Precipitation Calculator (OPIC) (Bowen, 2020; Bowen and Revenaugh, 2003)) from the transect endmembers (Ndabaka and Malambo Road) and midpoint (Makoma) of the transect. Color scheme is consistent with Figure 3. (b) Plot of $\delta^{18}O$ and δD from all waters analyzed for this study with the Global Meteoric Water Line (GMWL) shown in black, African Meteoric Water Line (AMWL) in red (Rozanski et al., 1996), and local meteoric water line (LMWL) in green (Otte et al., 2017). (c) Plot of $\delta^{18}O$ and d-excess from all waters analyzed for this study. Errors for $\delta^{18}O$ and δD are smaller than symbols.

Figure 5. (a) Plot of $\Delta'^{17}O$ and d-excess with symbols colored by water type. (b) Plot of $\Delta'^{17}O$ and d-excess of soil water ($\Delta'^{17}O_{sw}$ and d-excess$_{sw}$) with symbols colored by soil site (c) Plot of $\delta'^{18}O$ and $\Delta'^{17}O$ with symbols colored by water type. (d) Plot of $\delta'^{18}O$ and $\Delta'^{17}O$ of soil water ($\delta'^{18}O_{sw}$ and $\Delta'^{17}O_{sw}$) with a λ value (0.518) plotted for reference. Symbols colored by site. Refer to Figure 1 for locations. (a-d) $\Delta'^{17}O$ typical error of ±15 per meg indicated. $\delta'^{18}O$ and d-excess error less than width of symbol.

Figure 6. (a) Plot of $\delta^{13}C$ and $\delta^{18}O$ of soil carbonates ($\delta^{13}C_{sc}$, $\delta^{18}O_{sc}$) from this study along with the published data from modern soil carbonates available from elsewhere in Africa. Eastern Africa data are from Kenya, Ethiopia, and Tanzania and the rest of the data are from Libya and South Africa (Cerling and Quade, 1980; Passey et al., 2010; Salomons et al., 1978). The percent fractional woody cover and vegetation classification are noted by different background colors based on $\delta^{13}C_{sc}$ after Cerling et al. (2011). (b) $\delta^{18}O_{sc}$ plotted against depth. (c) $\delta^{18}O_{sc}$ plotted against depth.

Figure 7. (a) Plot of $\delta^{18}O_{rsw}$ (calculated using the $\delta^{18}O_{sc}$ values and $T_{\Delta 47}$ from Table 6) versus modeled mean annual $\delta^{18}O$ of meteoric water from OPIC (Bowen, 2020; Bowen and Revenaugh, 2003). (b) Plot of $\delta'^{18}O$ and $\Delta'^{17}O$ of reconstructed soil water ($\delta'^{18}O_{rsw}$ and $\Delta'^{17}O_{rsw}$) with typical evaporation slopes, λ, plotted for reference assuming two different starting compositions of unevaporated soil water of ($\Delta'^{17}O$ = 20 per meg and $\delta'^{18}O$ = -7‰ and -5‰). (c) Aridity Index (MAP/PET) versus $\Delta'^{17}O_{rsw}$. (d) Water Deficit (PET - MAP) versus $\Delta'^{17}O_{rsw}$. The x-axis is reversed so that the highest water deficits align with the greatest aridity in Figure 7C.

Tables

Table 1. Location, soil, and climate information

Table 2. Summary statistics from Hobo temperature logger record.

Supporting Information

Figure S1. (a) Schematic diagram where $\Delta'^{17}O$ represents the deviation of $\delta'^{17}O$ and $\delta'^{18}O$ from the equilibrium Global Meteoric Water Line (GMWL; λ_{ref} = 0.528). (b) Evaporation should cause a decrease in $\Delta'^{17}O$ values and an increase in $\delta'^{18}O$ compared to the observed range of global precipitation. See Section 2. for explanation of triple oxygen isotope notation. (c) Schematic illustrating how reconstructed water values for $\delta'^{18}O$ and $\Delta'^{17}O$ are calculated.

Figure S2. Representative examples of the soils described and carbonate morphologies identified in this study. (a) Sandy Inceptisol from the most arid region of the Serengeti, Shifting Sands. (b) Mollisol with abundant calcium carbonate in the profile and illuviated clay that the base from the Kirawira site. (c) Alfisol with significant accumulation of sesquioxides and abundant FeMn nodules from the Kemarishe site. (d) Mollisol with vertic properties including significant cracks extending to 40 cm depth and pedogenic slickensides. The Ndabaka site was only soil profile with pedogenic slickensides (e) Example of the range of sizes of pedogenic carbonate nodules present at the same depth at Ndabaka site. (f) Highly abundant carbonate nodules from the Simba Kopjes site with a popcorn like texture found at many of the sites. (g) Highly calcareous matrix and abundant soil carbonates from the Musabi site. (h) Carbonate coatings on a cobble of highly weathered igneous rock from Shifting Sands site. (i) Coalesced nodules forming a petrocalcic horizon at the Banagi site.

Figure S3. (a) $\Delta'^{17}O_{sw}$ plotted with depth. (b) $\Delta'^{17}O_{rsw}$ plotted with depth. (c) $\delta'^{18}O_{sw}$ plotted with depth. (d) $\delta'^{18}O$ plotted with depth. (e) d-excess plotted with depth. (a-e) colored by site.

Table S1. Soil temperature logger data.

Table S2. Carbon and oxygen isotopic data, description of carbonate morphology, and sampling procedure.

Table S3. Summary statistics of carbon and oxygen isotopes.

Table S4. Raw and corrected clumped isotope data for samples and standards.

Table S5. Summary of clumped and triple oxygen isotopic data organized by site and depth in soil.

Table S6. Standards summary and pooled standard deviation for triple oxygen isotopes and clumped isotopes.

Table S7. Triple oxygen isotope raw and corrected data for Reactor 4.2.

Table S8. Triple oxygen isotope raw and corrected data for Reactor 5.

Table S9. Triple oxygen isotope raw and corrected data for Reactor 6.

Table S10. Triple oxygen isotope raw and corrected data for Reactor 7.

Table S11. Triple oxygen isotope raw and corrected data for Reactor 8.

Table S12. Physical descriptions of soils.

Table S13. $\delta^{18}O$, δD, and $\Delta'^{17}O$ water data. Values in ‰VSMOW-SLAP unless otherwise indicated.

Table S14. Pairwise comparison of the measured soil temperature means.

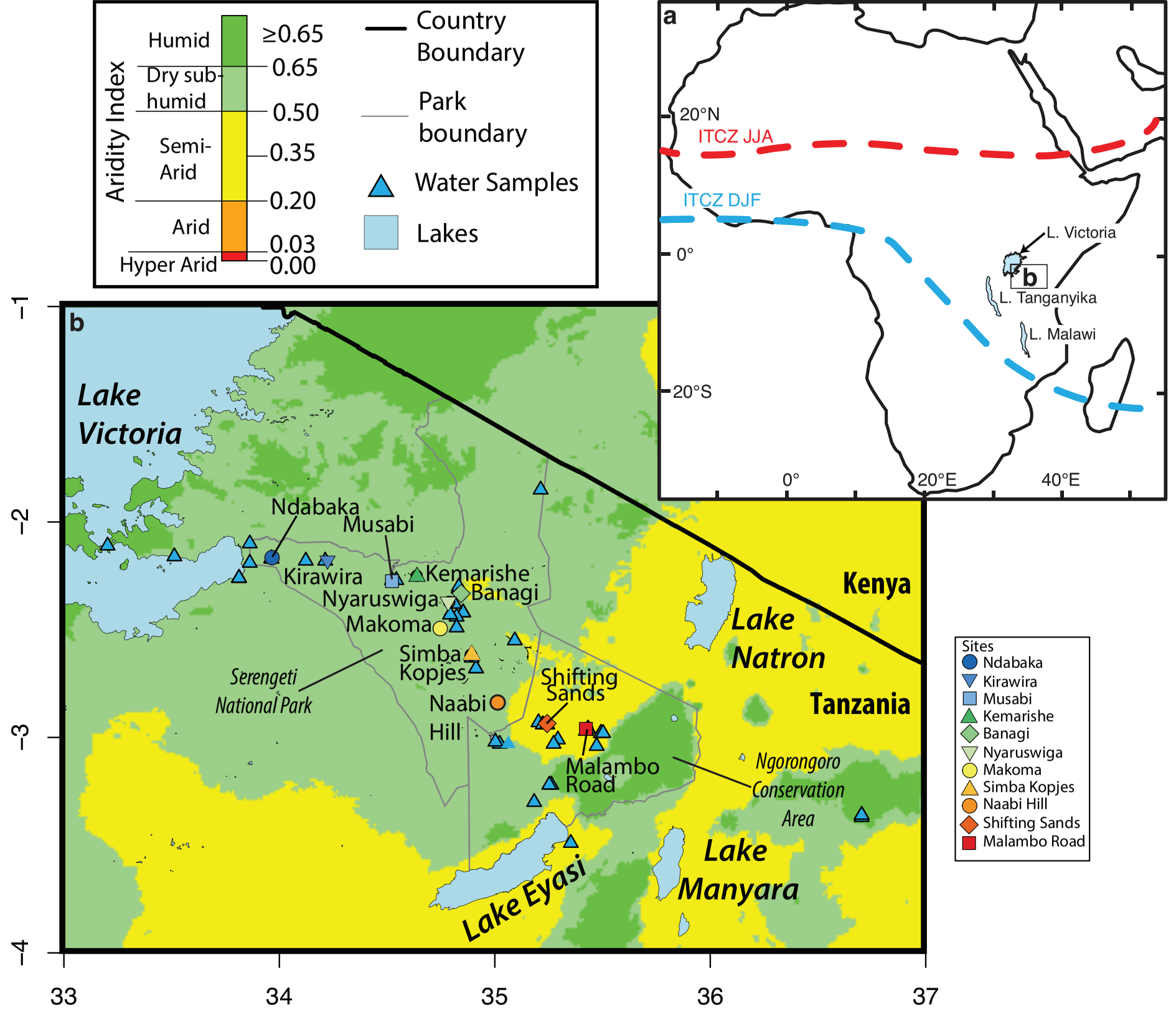

Figure 1

Click here to access/download;Figure;Figure 1 - Location Map.eps

Figure 2

Click here to access/download;Figure;Figure 2 - Temperatures and Clumped.eps

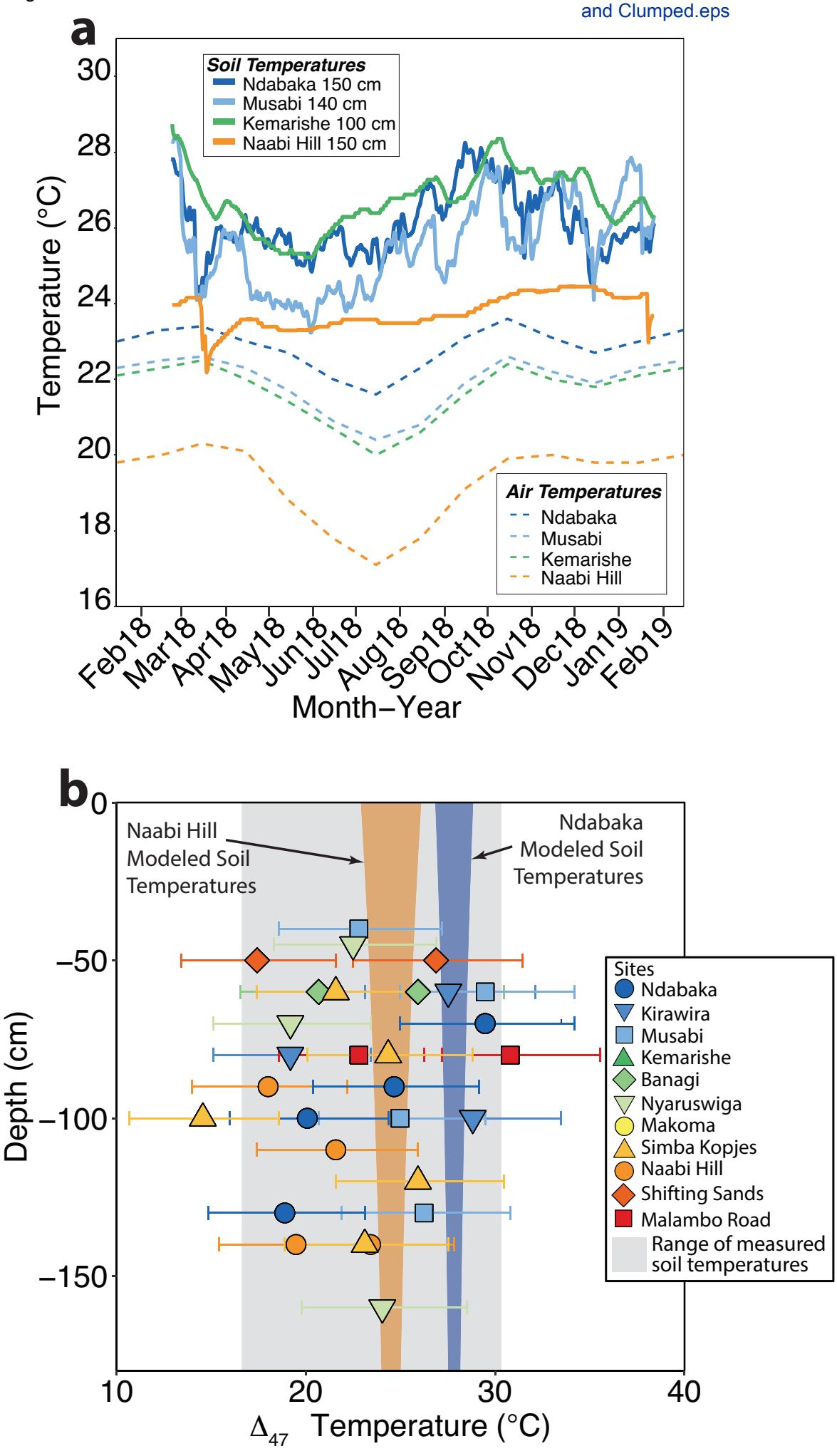

Figure 3

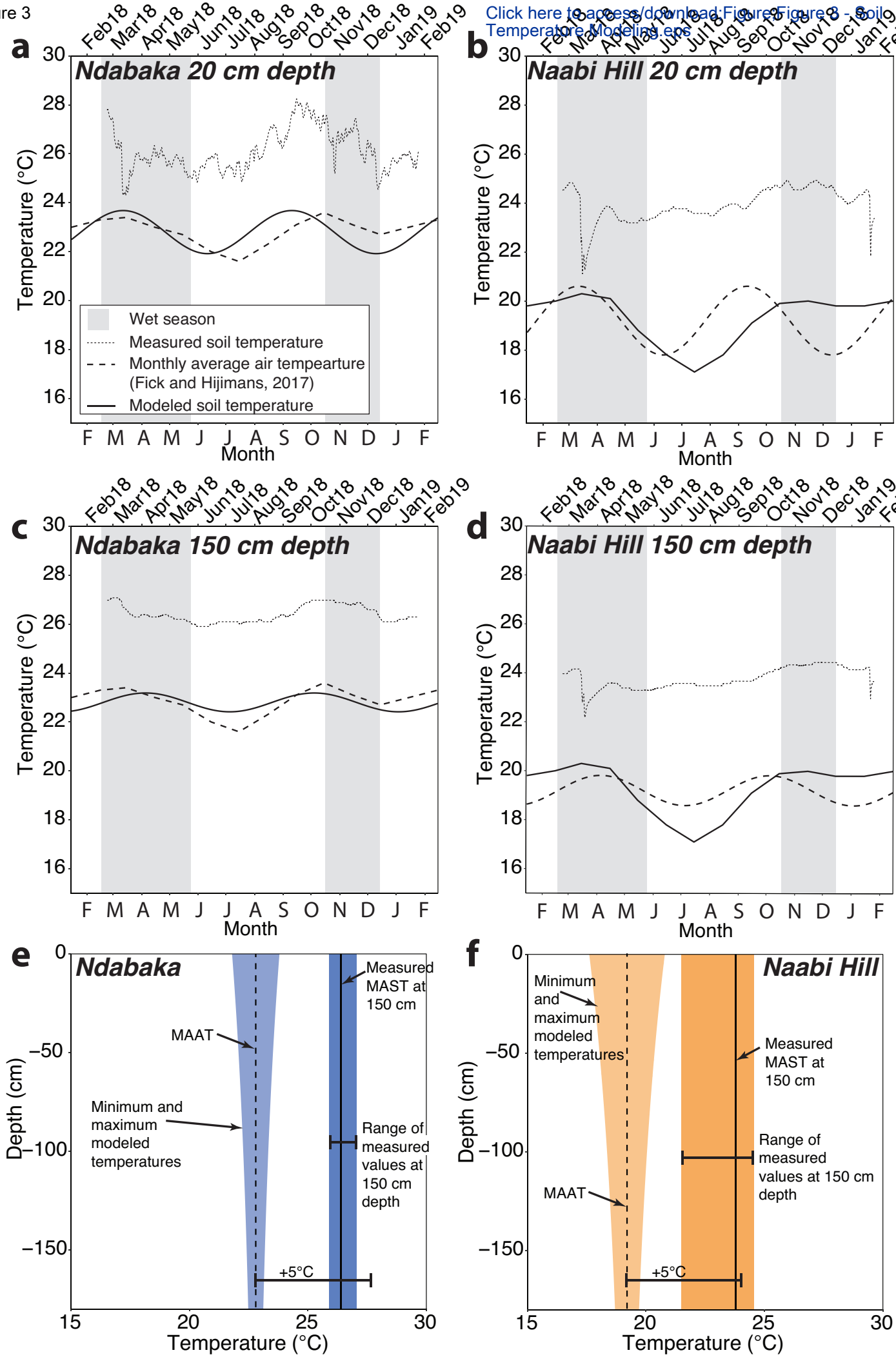

Figure 4

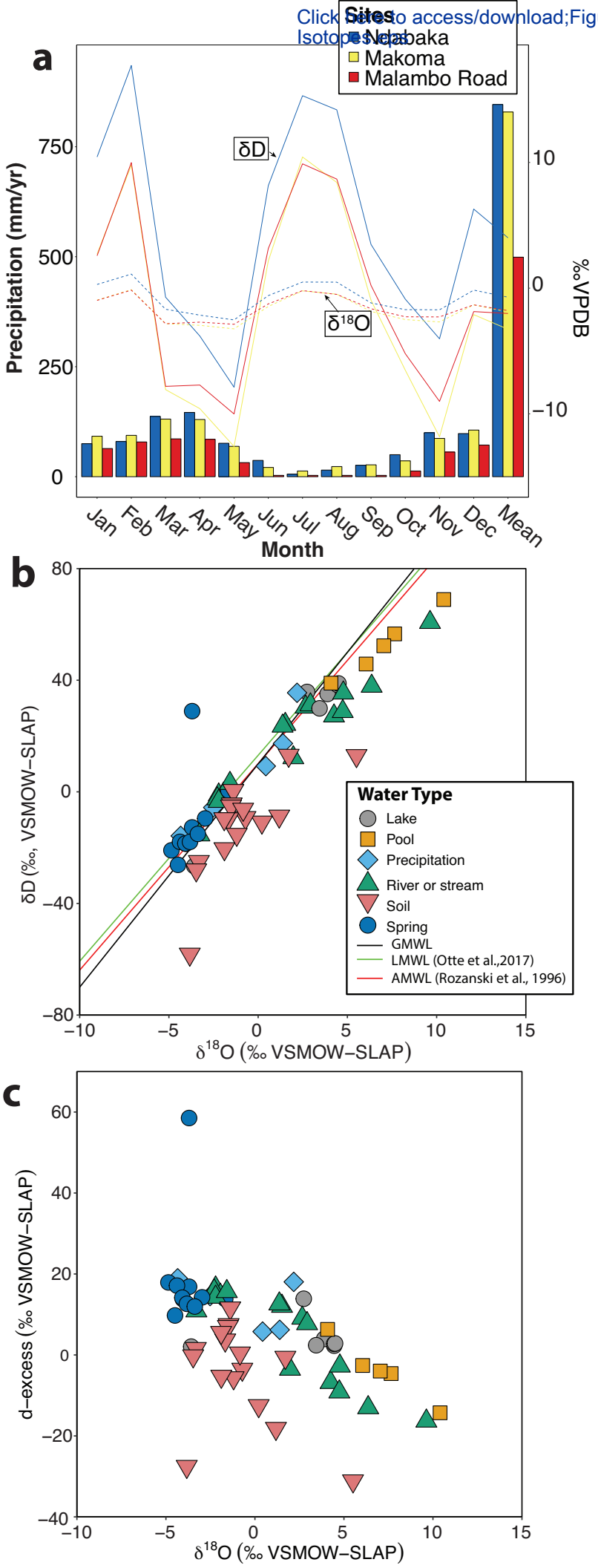

Figure 5

Click here to access/download;Figure;Figure 5 - 17O comparison.eps

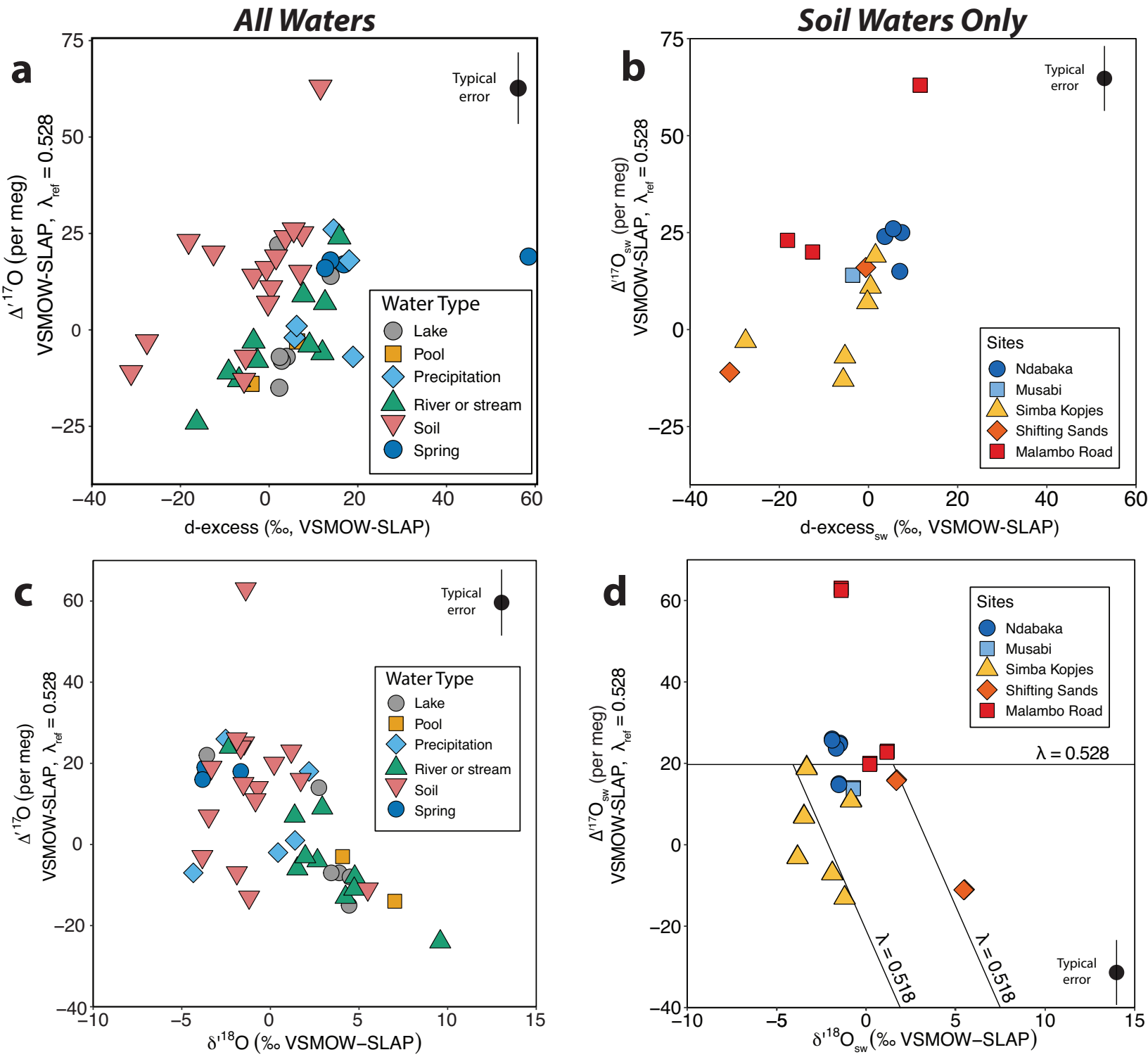

Figure 6

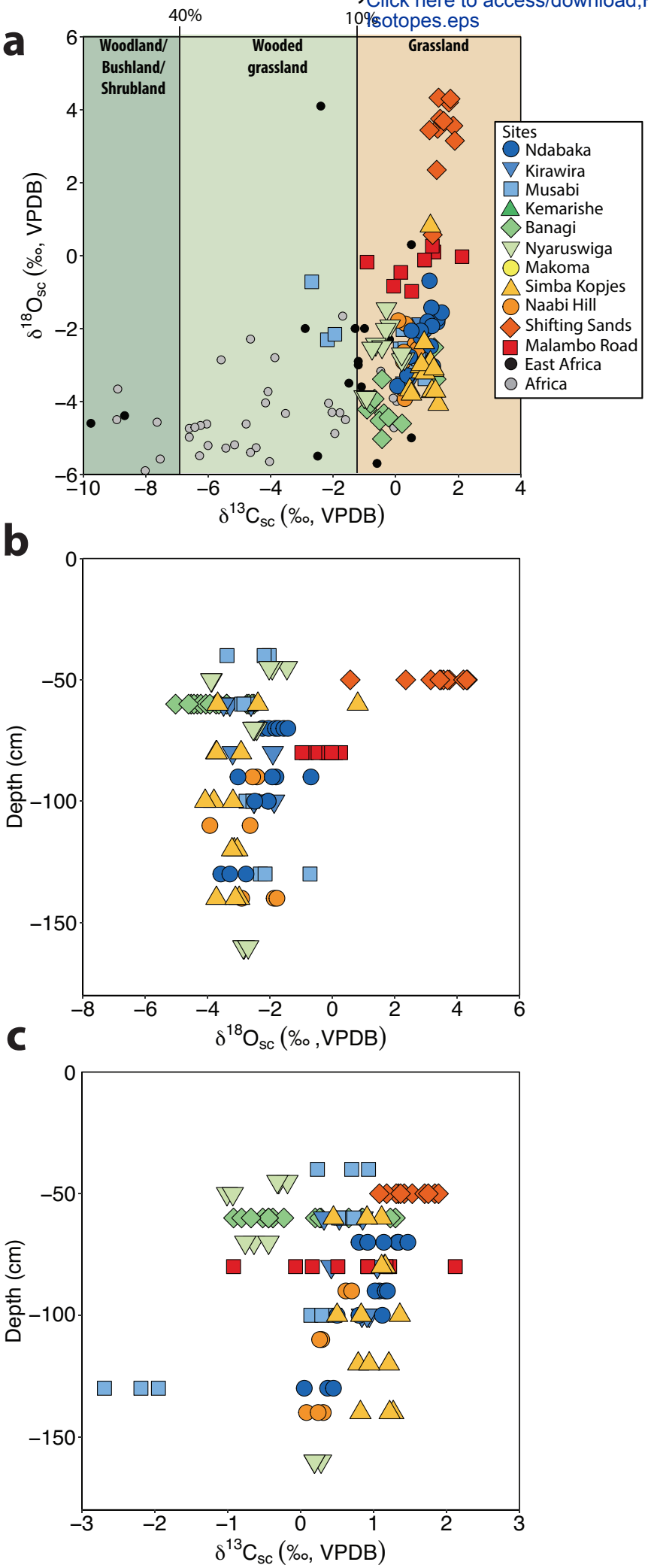

Figure 7

Click here to access/download;Figure;Figure 7- summary figures.eps

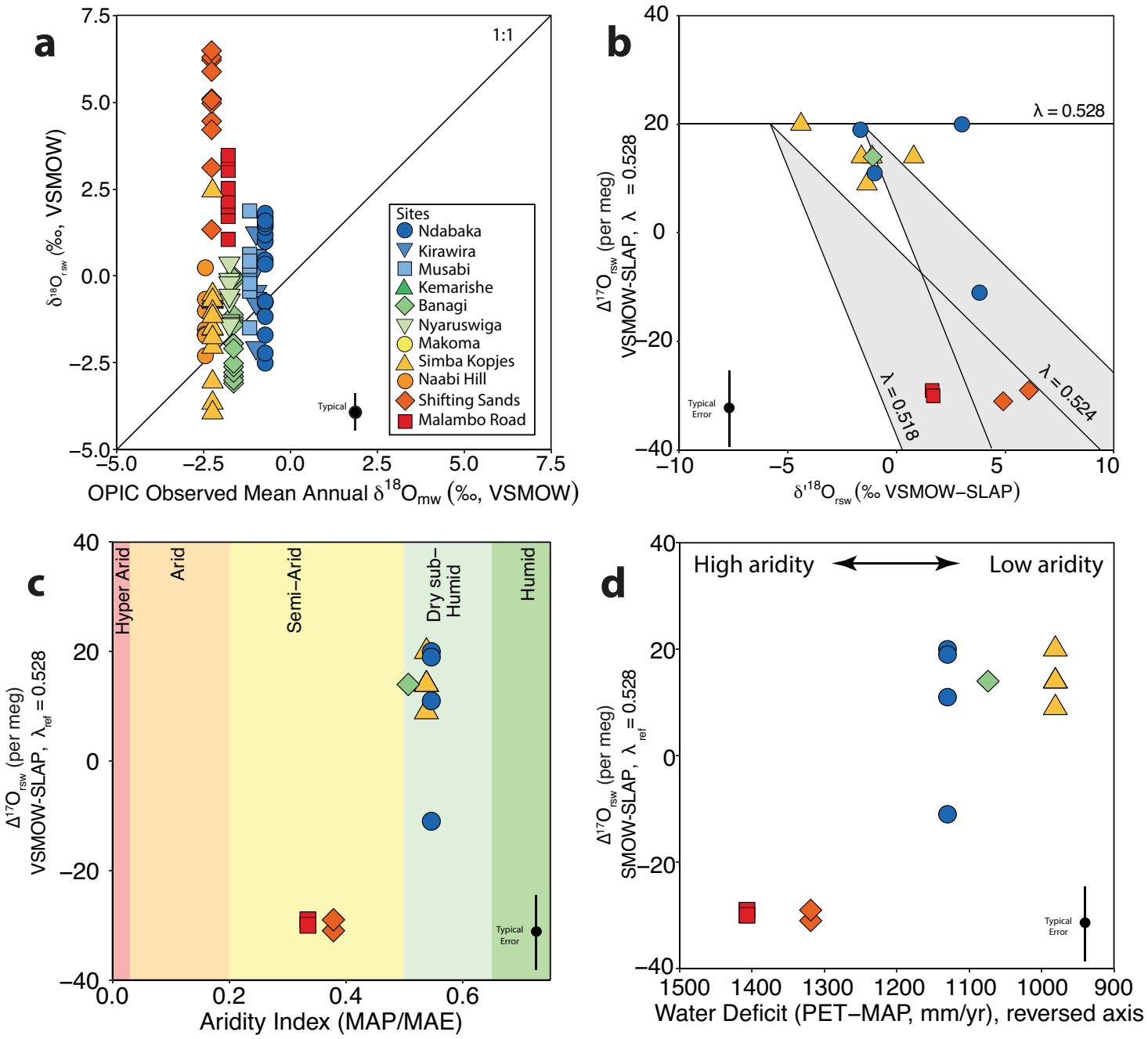

Table 1: Location, soil, and climate information.

Site	Latitude	Longitude[a]	Elevation (masl)[b]	Vegetation[c]	Soil Order[d]	MAT (°C)[e]	MTWQ (°C)[e]	MAP (mm/yr)[e]	PET (mm/yr)[f]	AI[f]	WD (mm/yr)[f]
Malambo Road	-2.9603	35.4364	1354	Dense grassland	Inceptisol	20.9	22.0	499	1583	0.33	1084
Shifting Sands	-2.9355	35.2473	1549	Dense shrubbed grassland	Inceptisol	19.8	20.9	558	1521	0.38	963
Naabi Hill	-2.8396	35.0205	1677	Closed shrubbed grassland	Mollisol	19.2	20.1	734	1486	0.52	752
Simba Kopjes	-2.6169	34.8966	1637	Dense to closed grassland	Mollisol	19.6	20.5	805	1521	0.54	716
Makoma	-2.4930	34.7544	1549	Closed treed shrubland	Inceptisol	20.2	21.0	829	1560	0.55	731
Nyaruswiga	-2.3496	34.8263	1451	Open treed grassland to closed grassland	Mollisol	20.8	21.6	832	1613	0.51	781
Banagi	-2.3290	34.8478	1425	Mixed open grassland to woodland	Inceptisol	20.9	21.8	819	1622	0.51	803
Kemarishe	-2.2498	34.6448	1315	Open grassed woodland	Alfisol	21.6	22.3	834	1659	0.5	825
Musabi	-2.2719	34.5339	1278	Closed grassland	Mollisol	21.9	22.5	830	1659	0.51	829
Kirawira	-2.1883	34.2322	1215	Dense to closed grassland	Mollisol	22.4	22.9	838	1655	0.53	817
Ndabaka	-2.1654	33.9734	1153	Dense to closed grassland	Vertic Mollisol	22.8	23.2	846	1642	0.55	796

[a]datum WGS 1984

[b]meters above sea level

[c]Vegetation from Reed et al. (2009)

[d]Soil Order identified based on field observations and climate, to provide a general understanding of soil type, but is not intended to be an absolute USDA soil classification

[e]MAT = Mean Annual Temperature, MTWQ = Mean Temperature Warmest Quarter, MAP = Mean Annual Precipitation from Fick and Hijmans (2017)

[f]PET= Potential Evapotranspiration, AI = Aridity Index, and WD = Water Deficit from Zomer et al. (2007,2008).

Table 2: Summary statistics from Hobo temperature logger record.

Site	Depth (cm)	Min T (°C)	Max T (°C)	Mean T (°C)	SD	Variance
Ndabaka	20	24.16	28.46	26.11	0.86	0.74
Ndabaka	80	25.51	27.66	26.41	0.58	0.34
Ndabaka	150	25.90	27.07	26.40	0.35	0.12
Musabi	40	21.57	28.46	25.51	1.19	1.42
Musabi	140	24.93	27.27	25.90	0.58	0.33
Kamarishe	30	23.48	30.15	26.39	1.38	1.89
Kamarishe	100	25.22	29.25	26.73	0.78	0.62
Naabi Hill	20	16.71	28.36	24.13	1.73	3.00
Naabi Hill	90	19.95	24.93	23.93	0.68	0.46
Naabi Hill	150	21.95	24.55	23.78	0.44	0.20

Figure S1

Figure S2

Figure S3

Figure S4

Table S1

Table S2

Table S3

Table S4

Table S5

Table S6

Table S7

Table S8

Table S9

Table S10

Table S11

Table S12

Table S13

Table S14